Ever J. Barbero and Antoine Joseph Bedard Jr., Electrical percolation threshold of magnetostrictive inclusions in a piezoelectric matrix composite as a function of relative particle size, Computational Particle Mechanics, (2018) vol. 5(2), pp. 227-238. DOI: 10.1007/s40571-017-0165-4

Electrical percolation threshold of magnetostrictive inclusions in a piezoelectric matrix composite as a function of relative particle size

Ever J. Barbero, Antoine Joseph Bedard Jr.

ABSTRACT

Magnetoelectric composites can be produced by embedding magnetostrictive particles in a piezoelectric-matrix derived from a piezoelectric powder precursor. Ferrite magnetostrictive particles, if allowed to percolate, can short the potential difference generated in the piezoelectric phase. Modeling a magnetoelectric composite as an aggregate of bi-disperse hard shells, molecular dynamics was used to explore relationships among relative particle size, particle affinity, and electrical percolation with the goal of maximizing the percolation threshold. It is found that two factors raise the percolation threshold, namely the relative size of magnetostrictive to piezoelectric particles, and the affinity between the magnetostrictive and piezoelectric particles.

Key words: magnetostrictive, piezoelectric, magnetoelectric, percolation, granular molecular dynamics, LAMMPS, particle segregation, particle size, polydisperse hard shells, Leonard-Jones

1. Introduction and objectives

Magnetostriction is a property of ferromagnetic materials that causes them to deform with strain when exposed to a magnetic field [1-8]. For example, Cobalt ferrite $CoFe_2O_4$ (CFO) is a ceramic ferrite with high magnetostrictive coupling [5]. The piezoelectric effect [4, 7] is the ability to generate electrical potential in response to an applied mechanical strain [9]. For example, perovskite $Pb[Zr_{0.52}\ Ti_{0.48}]O_3$ (PZT) is a chemically stable and hard material with high piezoelectric coupling [10]. Magnetoelectric (**ME**) composites combine magnetostrictive and piezoelectric materials into a composite material that can convert a magnetic field into an electrical potential [1-8].

Since magnetostrictive (**H**) materials are electrically conductive [1-3], once the **H** particles percolate, the charge produced by the piezoelectric (**E**) materials is lost, so a high percolation threshold is needed to achieve high magnetoelectric performance [11-16]. Therefore, the objective of this study is to find the largest volume fraction for which electrical percolation of the **H** phase does not occur as a function of the relative particle size and affinity between the precursor powders.

The ratio of the volume of **H** particles to the volume of the simulation box is denoted by $\boldsymbol{\rho} = V_H/\text{box volume}$. A mixture of two powders, one conductive and the other insulating, represented by spheres of equal diameter has a percolation threshold of $\boldsymbol{\rho_c}$ =15.4 % regardless of the arrangement of the spheres into any type of lattice [11, 17]. The volume ratio $\boldsymbol{\rho}$ may be written as $\boldsymbol{\rho = f \times p}$ where **f** is the packing fraction of both powders in the container, and $\mathbf{p} = V_H/(V_H+V_E)$ is the volume fraction [17]. If the interstitial space between the **H** spheres is filled completely by the **E** phase, then **f**=1, and the volume ratio $\boldsymbol{\rho}$ and the volume

fraction **p** are numerically equal. However, if the interstitial space between **H** particles is reduced by sintering, then the volume fraction increases because $\mathbf{p_c = \rho_c/f}$ where **f** is measured before sintering.

Others have studied the effects of particle size on rheology or flow patterns [18, 19] and granular segregation [20, 21], and numerous researchers have applied molecular or particle dynamics to the study of granular motion [18-21]. Kuzy [23] studied the effects of particle size on granular static spatial distribution patterns and, in particular, studied the percolation threshold when $\mathbf{\rho_c = p_c}$ of a fine-grain conductive phase **H** with spherical particle radius $\mathbf{R_H}$ dispersed and surrounding larger spherical particles of insulating phase **E** with radius $\mathbf{R_E}$. He concluded (Fig. 1 lower right insert) that the larger the $\mathbf{R_E/R_H}$ ratio, the lower the percolation threshold of the **H** phase. Our study is the diametric opposite of Kuzy's; that is, to increase the percolation threshold of the larger **H** phase (Fig. 1 upper left insert) by reducing the size of particles in the **E** phase. One goal of this study is to test via molecular dynamics simulation the proposition that the percolation threshold of the **H** phase will increase as the size of the particles in the **E** phase decreases [11-12, 20, 23, 24].

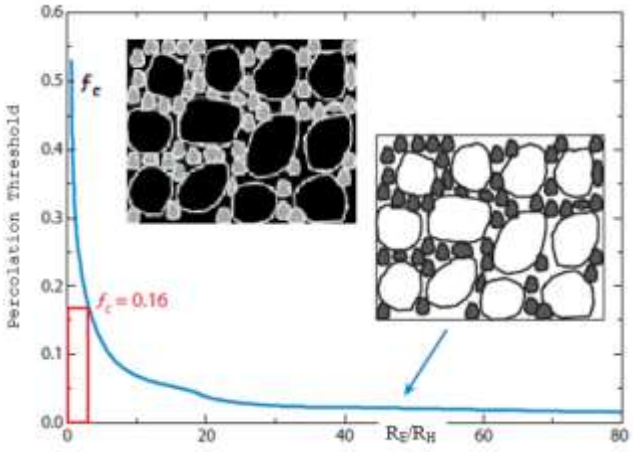

Fig. 1. Percolation threshold prediction form [11] as a function of relative particle size R_E/R_H. Insert lower right: smaller H dark particles; upper left: larger H dark particles.

2. Methodology

2.1 Molecular Dynamics

In this study, molecular dynamics is preformed using Large Scale Atomic and Molecular Massively Parallel Simulation (LAMMPS)© software from Sandia National Laboratories [34] to simulate the mixing of two powders that represent the magnetostrictive **H** and piezoelectric **E** phases. Particles are modeled as perfect spheres of uniform density for each phase, but each phase has a different diameter with a ratio between the two diameters given by $\mathbf{R_H/R_E}$. The Leonard-Jones (L-J) "12-6" potential is used in this study to model particles interactions where distance is expressed in units of sigma ($\boldsymbol{\sigma}$) and energy in units of epsilon ($\boldsymbol{\varepsilon}$) which are features of the pair-wise L-J potential function between particles centers (Fig. 2). The diameter D the **H** particles were chosen to be 100 nm ($D=1.12246\sigma$) as a compromise between the effects of quantum tunneling [25-31] and mechanical coupling [1-2, 13-16]. If the particles are too large,

mechanical coupling between the **E** and **H** phase will be poor. If the particles are too small, quantum tunneling will short any voltage produced in the **E** phase. The L-J potential can be used to model hard shell spheres with the particle diameter modeled as the cutoff corresponding to the deepest point in the well which is located at 1.12246σ (Fig. 2). The potential after the cutoff value $\mathbf{R_c}$ is set to zero.

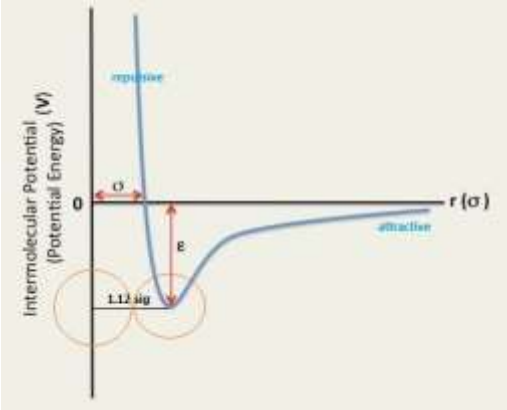

Fig. 2 Leonard-Jones pair-wise potential energy.

To approximate the hard-shell behavior, the well depth (Fig. 2) was set to 10ε during the mixing stage and 20ε during the equilibration and gelation stages. Per preliminary studies using Hertzian analysis [32, 33] to compare Leonard-Jones well depth to particle elasticity, a well depth of 10ε to 20ε produces a stress which is at least three orders of magnitude larger than any stress which would be produced by gravity on either the **H** or **E** particles. Therefore, the effects of gravity may be ignored. To simulate particle friction and affinity, an attractive force is added between the **H** and **E** particles while no other forces are present. This was accomplished by extending the L-J cutoff between the **H** and **E** particles from $\mathbf{r_{co}}$ =1.12246σ to $\mathbf{r_{co}}$ = 1.25σ. The value 1.25σ was chosen because too large a cutoff violates the rigid spheres assumption that particles do not attract each other. If particles attract each other over long distances, then the distance between the particles decreases, thus enhancing the likelihood of **H** particle percolation, contrary to our goals.

2.2 Simulation Process

We require **H** and **E** particles to be well mixed with each other to maintain high electromechanical energy transfer between them. All simulations are time integrated with the Verlet velocity algorithm [34] using the Nose-Hoover NVT thermostat where the number and volume are fixed and temperature is either fixed or slowly decreased. To prevent segregation, a common problem when mixing powders [23, 35-40], the simulations are performed in three separate stages of mixing, equilibration, and gelation.

In the first stage (mixing) all particles are initially mixed at an L-J temperature of $T=0.2\ \varepsilon/k_B$ (k_B is the Boltzman constant) for 10 million time steps for R_H/R_E=1, 2, and 5 million time steps for R_H/R_E=3. In all cases, periodic boundary conditions are applied. For equally sized spheres, the maximum packing fraction below which the particles are free to move is **f**=0.64 [39]. For any packing fraction above this value, the particles will experience a glass transition [36, 39] and thus are not be able to move or mix. Therefore, for the mixing stage, the packing fraction used was **f**=0.5236 corresponding to the simple cubic (sc) lattice. This is sufficiently less than **f** =0.64 to allow mixing to occur.

The second stage (equilibration) is where local particle movement on the order of particles size is allowed, but motion on the order of the size of the simulation box is restricted. The equilibration stage is run for 100,000 time steps with the L-J parameters $\boldsymbol{\sigma}$ and the cutoff $\mathbf{r_{co}}$ adjusted to increase the particle size, so that the particles occupy more space for a fixed simulation box volume, effectively increasing the packing fraction from **f**=0.5236 to **f**=0.553. During the second stage (equilibration) the simulation is run at a cold temperature ramped from $T=0.02\varepsilon/k_B$ to $0.01\varepsilon/k_B$ allowing sufficient energy for the particles to move locally to find their equilibrium positions but restrict particle movement sufficiently to avoid particle segregation [23, 35-40]. Finally, the third stage (gelation) is run for 10,000 additional time steps where the temperature is also ramped from $T= 0.02\varepsilon/K_B$ to $0.01\ \varepsilon/k_B$, to allow sufficient energy for motion while the L-J interaction between the particles and the box walls is adjusted to effectively decrease the box size to achieve the target packing fraction of **f**=0.64, 0.675, 0.73 for R_H/R_E = 1, 2, 3 respectively [39].

2.2.1 Packing Fraction

To achieve a packing fraction of **f**=0.64, 0.675, or 0.73, for R_H/R_E=1, 2, 3, without segregation, particles of diameter 1.12246σ are mixed in a simulation box of side length equal to $20\times1.12246\sigma$ at a packing fraction of 0.5236 with periodic boundary conditions applied. In the equilibration stage, isotropic compression [20] is applied to scale up the particle radii by a factor of $(0.64/0.5236)^{1/3}$ for R_H/R_E=1, $(0.675/0.5235)^{1/3}$ for R_H/R_E=2, and $(0.73/0.5235)^{1/3}$ for R_H/R_E=3. For R_H/R_E=1 this scale factor would increase the packing fraction to $0.5236 \times (0.64/0.5235) = 0.64$. However, with periodic boundary conditions the particle centers can reach the walls of the box, effectively decreasing the packing fraction to $0.64 \times(20/21)^3 = 0.552856$. This packing fraction is still sufficiently below **f**=0.64, to allow local particle movement, but is sufficiently high to prevent phase segregation, as evidenced by the measurements for the center of mass (CoM), average local volume fraction ($\mathbf{p_a}$), probability density profile (PDP), and radial distribution function (RDF) (see section 2.3). To restore the packing fraction back to 0.64 the simulation box is shrunk by a factor of (20/21) in the gelation stage, thus removing the reduction in packing fraction **f** that resulted from using periodic boundary conditions.

2.2.2 Particle Size

Simulations were conducted for three relative particle sizes of R_H/R_E =1, 2, 3 where R_H and R_E are the radius of the conductive **H** and insulating **E** phase particles, respectively. R_H is fixed at 100 nm, and the density of the particles is scaled to correspond to CFO and PZT molecular weights. When the **H** and **E** particles are of equal size, the simulation box side length is 1.12246σ times the cube root of the number of particles being simulated. Specifically, for 20^3 total spheres the length of the simulation box is $1.12246\sigma\times20 = 22.4492\sigma$. Since the size of the box and the number of **H** particles remains unchanged throughout this study, to maintain the volume fraction (**p**) and the packing fraction (**f**) unchanged, the number of **E** particles is varied with $(R_H/R_E)^3$. In the gelation stage, the simulation uses rigid walls which are constructed with Leonard-Jones particle-wall interactions equal to the particle-particle interactions.

2.3 Characterization

Measurements for this study include the radial distribution function (RDF), probability density profiles (PDP), center of mass (CoM), and average local volume fraction ($\mathbf{p_a}$), which were used to characterize the degree of mixing.

2.3.1 Radial Distribution Function

The radial distribution function (RDF) maps the distances among pairs of particles **H-H**, **E-E**, and **H-E** to the likelihood of finding pairs of particles at those distances from each other. These functions characterize the structure between phases as well as mean separation distances which are a key parameter for understanding percolation [12, 25, 41, 42, 55].

2.3.2 Probability Density Profiles

Probability density profiles (PDP) are histograms of the number of particles (both **H** and **E**) which in this study are computed between y and y+Δy along the y axis of the simulation box, where Δy represents the histogram bin size which is taken as one eight the length of the simulation box. The PDP gives a measure of the degree of mixing between **H** and **E** particles. The percent difference is defined as the difference between the maximum and minimum values of density divided by the average density. Percent differences less than 10 % typically indicate good mixing. On the other hand if the particles segregate, a sharp inflection or abrupt value change in the PDP is observed.

2.3.3 Center of Mass

The center of mass (CoM) is computed as a function of time in L-J time steps along a single direction of the simulation box for the H particles only. A well-mixed distribution of **H** particles will have a CoM within plus or minus 5 % of the center of the box after the simulation is completed. A CoM outside this 5 % range provides an indication that segregation has occurred.

2.3.4 Average Local Volume Fraction

The average local volume fraction ($\mathbf{p_a}$) is an intrinsic scale invariant quantity proportionate to the volume fraction measured repeatedly within small spheres of radius twice the radius of an **H** particle for all particles both **H** and **E** for any given simulation. For example, for a simulation with volume fraction p=0.18, if 12 **H** particles of diameter **D** were found in a sphere of diameter 2**D** centered around any given particle, and 64 **E** particles were found in that same sphere, then $\mathbf{p_a}$ for that point would be $12/64 \times 100 = 0.1875$. This calculation is repeated for all particle centers and averaged. In order to compare $\mathbf{p_a}$ values for simulations of unequal number of **E** particles, the number of **E** particles is normalized by dividing the number of **E** particles found in any 2**D** sphere by $(R_H/R_E)^3$.

2.4 Percolation Distance

The percolation distance $\mathbf{R_c}$ or critical range between particle centers where percolation first occurs is the *smallest* distance between adjacent particle centers for which pairs of connected particles are chained together to produce a percolation path from one side of the simulation box to the other. Any distance larger than $\mathbf{R_c}$ will also produce a percolation path, but the critical percolation distance is always the smallest distance among coordinate centers which produces a percolation. The percolation distance $\mathbf{R_c}$ includes the effective particle diameter after growth (section 2.4.1) and the effect from quantum tunneling (section 2.4.2). Because the growth or scaling factor is different for different packing fractions at which glass transition is expected, $\mathbf{R_c}$ is calculated as follows:

$\mathbf{R_c}$ = particle diameter × scale factor × quantum tunneling (1)

$R_H/R_E=1 \rightarrow R_c = 1.12246\sigma \times (0.64/0.5236)^{1/3} \times 1.05 = 1.26\sigma$ (1a)

$R_H/R_E=2 \rightarrow R_c = 1.12246\sigma \times (0.675/0.5236)^{1/3} \times 1.05 = 1.28\sigma$ (1b)

$R_H/R_E=3 \rightarrow R_c = 1.12246\sigma \times (0.73/0.5236)^{1/3} \times 1.05 = 1.32\sigma$ (1c)

2.4.1 Particle Growth Factor

The maximum packing fraction of equally sized random close packed spheres that can be achieved without particle deformation is **f** = 0.64 for $R_H/R_E = 1$, **f** = 0.675 for $R_H/R_E = 2$, and **f** = 0.73 for $R_H/R_E = 3$ [38, 39]. When powders or hard shell spheres are mixed, segregation between non-identical particles can occur when the particles are under stress or pressure [23, 35-40]. In order to achieve a packing fraction of **f** = 0.64 while avoiding phase segregation, in the case of $R_H/R_E=1$, the particle diameters are increased in the equilibration stage by a scaling factor of $(0.64/0.5235)^{1/3} =1.069203$. This increases the diameter of the particles from 1.12246σ to 1.200137σ. In the case of $R_H/R_E=2$, and 3, the particle diameters are increased by a factor of $(0.675/0.5235)^{1/3}$, and $(0.73/0.5235)^{1/3}$ respectively (section 2.2.1).

2.4.2 Quantum Tunneling

Quantum tunneling [43] is an effect whereby electric charge can jump a space between conductive but electrically isolated particles that is forbidden by classical mechanics. Quantum tunneling is reported to range from 3 nm [25] to 10 nm [31] between conducting particles in a non-conducting matrix. Others [28, 29] describe plasmonic (charge density) energy transfer partially attributed to tunneling between conducting particles separated by distances up to 7 nm. Hill et al. [27] reports plasmonic conduction between particles exceeding a separation distances of 20 nm. As a compromise among the values reported in the literature, a quantum tunneling distance of 5 nm is added to the distance $\mathbf{R_c}$ between particles centers which is used to evaluate percolation. For **H** particles with diameter D=100 nm, this is represented by the factor 1.05 shown in eqns. (1).

2.5 Percolation

A novel algorithm was developed to detect percolation. The algorithm consists of two subroutines. The first subroutine builds a pair-bonding list of all pairs of **H** particles that are less than $\mathbf{R_c}$ from each other. The second subroutine attempts to find a path from the particles located near one side of the box to those located near the other side by chaining together successive pairs of particles via recursion [44]. Particles are considered to be near a wall of the simulation box if their centers are located within 10 % of the length of the simulation box.

After $\mathbf{R_c}$ is determined for a given volume fraction **p**, the average random close packed coordination number **c.n.** is computed and later used to show that the average number of connections of each particle to nearby particles within a distance of $\mathbf{R_c}$ is approximately independent of the volume fraction **p**. An end zone distance of 10 % was chosen because the particles centers cannot get closer than 0.627σ from either simulation wall adjusting for particle growth in the equilibration stage. This causes a dearth of particle

centers in the first and last slice closest to the walls as shown in Fig. 5 (section 3.2). Since the box length is 22.4492σ, 10 % of this is rounded to 2.25σ. The second to last slice where a full population of particles is expected to occur is between 0.63σ and 1.9σ. Adding a small safety factor of 0.35σ to account for steric effects, if any percolation path gets within 2.25σ or 10 % of the box length to a wall, a conductive path is presumed.

2.6 Affinity

As all the particles are compressed, for the cases when $\mathbf{R_H/R_E}$ is not equal to one, the smaller **E** particles are likely to move to the interstitial space between the large **H** particles rather than maintain positions that separate **H** particles from each other. Friction between the **H** and **E** particles would reduce this tendency, but the Leonard-Jones potential used in this study produces a purely radial force between particles without a shear or frictional component. The effect of friction may be partially simulated, however, by a radial attractive force between the **H** and **E** particles. A radial force between the **H** and **E** particles is implemented by extending the L-J cutoff parameter $\mathbf{r_{co}}$ between the **H** and **E** particles. In our study, we extended the L-J from $\mathbf{r_{co}} = 1.12246\sigma$ to $\mathbf{r_{co}} = 1.25\sigma$. The value 1.25σ was chosen to allow the **H** particles to attract the **E** particles close to the surface of the **H** particles, but to be short range enough so as not to allow long range forces to do work on the system.

In addition, even in the absence of friction, a slight attractive force between **H** and **E** particles allows the smaller **E** particles to act like a coat of paint surrounding and insulating the conductive **H** particles which would increase the percolation threshold. Functionalization of CFO particles into polymers has been considered by [45] whereby similar techniques might be used to produce affinity between **H** and **E** particles.

3. Results

The critical percolation threshold $\boldsymbol{\rho_c}$ of phase **H** is expressed as $\rho_c = V_H/V_{box} = f \times p_c$ where **f** is the packing fraction, $\mathbf{V_H}$ is the volume of the H particles, $\mathbf{V_{box}}$ is the volume of the simulation box, and $\mathbf{p_c}$ is the critical volume fraction, where volume fraction is defined as $p = V_H/(V_H+V_E)$. The critical percolation threshold $\boldsymbol{\rho_c}$ for equally sized hard-shell spheres without affinity is 0.1557 [11, 17]. To verify our model, three different lattices, simple cubic (sc) (**f**=0.5236), body centered cubic (bcc) (**f**=0.6802), and hexagonal close packed (hcp) (**f**=0.7405) were evaluated for percolation. For all crystal lattices, $R_H/R_E=1$, and different volume fractions were achieved by randomly removing a precise number of phase **H** spheres at lattice points while leaving the remaining **H** spheres in place. The results are shown in Table 1 and are comparable to Table I of [17].

For $R_H/R_E=1$, volume fraction is

$$p = N_H / (N_H+N_E) = V_H/(V_H+V_E) \qquad (2)$$

where N is the number of particles and V is the volume of phases E and H.

In general, the volume ratio is

$$\rho = f \times p \qquad (3)$$

The percolation thresholds $\mathbf{p_c}$ and $\boldsymbol{\rho_c}$ shown in Tables 1-2 are the lowest values of **p** and **ρ** for which percolation occurs.

Table 1. Percolation Thresholds for hcp, bcc, and sc lattices with $R_H/R_E=1$.

Crystal 3D	**c.n.**	**f**	$\mathbf{p_c}$	$\boldsymbol{\rho_c}$	$\boldsymbol{\rho_c}$ Scher-Zallen [23]
hcp	12	0.7405	0.175	0.130	0.144
bcc	8	0.6802	0.24	0.163	0.163
sc	6	0.5326	0.32	0.168	0.162

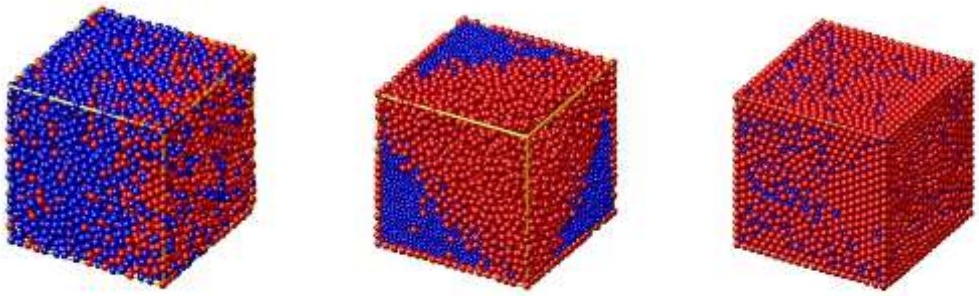

Fig. 3 Three different cases of segregation between red **H** and blue **E** particles

3.1 Segregation

When granular mixtures with different properties are subjected to stress or pressure, segregation as shown in Fig. 3 can occur [36, 46]. Segregation occurs between the different constituents [13-16, 23] [36, 47-50] due to difference in velocity, size, and density of the different particles groups. Segregation is detrimental to electromechanical coupling which requires the **H** and **E** particles to be thoroughly mixed. Percolation among one phase will either be undesirably enhanced within an aggregation of **H** particles which excludes **E** particles, or percolation will be inhibited if an agglomeration of **H** particles does not reach from one side to the other, but occupies just a central region. In this study, glass transition [35, 36, 41, 48, 51, 52] is used to restrict particle motion preventing segregation while the particles undergo equilibration and gelation. Glass transition is described as a sharp change from a viscous, rubbery, or fluid state to solid or gel state [35, 37, 52]. In this study we adopt the approach per [52] that at high packing fractions "arrest takes place via a glass transition process which can be driven by jamming as in hard sphere systems."

3.2 Random Close Packed Powders

The closest that hard spheres can be packed into any lattice are with a coordination number of 12 and packing fraction of 0.7405 [53] which occurs for hcp and fcc lattices. If a lattice is relaxed and the spheres are allowed to move randomly, the arrangement with the highest packing is called random close packing (rcp) with a packing fraction of 0.64 [17, 22, 37, 38, 40].

The results for simulations of random close packed powders using our methodology are shown in Table 2 and Fig. 4 with affinity (A) or no affinity (N) applied between **H** and **E** particles. The average local volume fraction $\mathbf{p_a}$ described in section 2.14 is a measure of mixing. When mixing between the **H** and **E** phases is well maintained the average local volume fraction $\mathbf{p_a}$ approaches **p** (or $\mathbf{p_c}$ at percolation). **c.n.** is the average coordination number of the **H** particles computed at the smallest inter-particle distance between **H** particle-centers that produces a percolation**.** $\mathbf{p_c} = V_H/(V_H+V_E)$ is the percolation threshold measured as the volume fraction of **H** with respect to the total volume of particles. $\boldsymbol{\rho_c} = V_H/\text{box}$ is the percolation threshold measured as the volume ratio of **H** to the simulation box. The latter is the value most commonly reported in the literature.

Table 2. Mean value and (COV [%]), $\mathbf{p_a}$: average local volume fraction, $\mathbf{p_c}$: percolation volume fraction, **c.n.**: coordination number, $\boldsymbol{\rho_c}$: percolation threshold, all results from n=3 simulations for each case.

Affinity	R_H/R_E	p_a	c.n.	p_c	ρ_c
N	1	0.2429 (10.19)	1.69 (16.22)	0.2433 (8.555)	0.1557 (8.384)
N	2	0.2780 (4.893)	2.02 (7.967)	0.2833 (5.391)	0.1913 (5.589)
N	3	0.3213 (3.962)	1.897 (3.390)	0.320 (5.413)	0.2337 (5.436)
N	4	0.3296 (0.4076)	1.953 (3.331)	0.3267 (1.767)	0.2467 (1.638)
A	1	0.2996 (2.165)	1.563 (9.320)	0.2967 (1.946)	0.190 (1.823)
A	2	0.3375 (2.923)	1.7467 (4.936)	0.350 (2.857)	0.2363 (2.753)
A	3	0.3984 (6.305)	1.55 (0.0)	0.3933 (5.292)	0.287 (5.273)
A	4	0.3639 (2.124)	1.757 (1.999)	0.3567 (3.219)	0.269 (3.219)

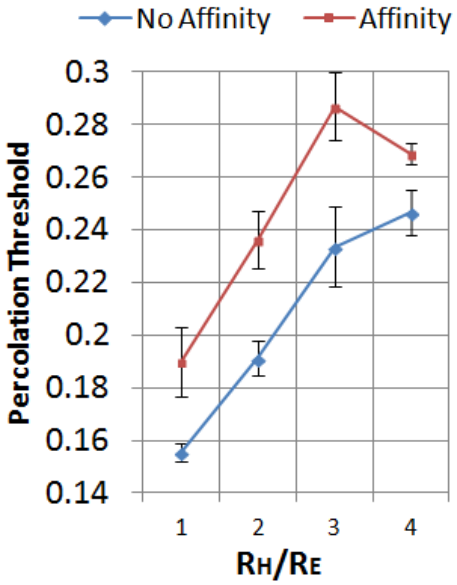

Fig. 4. Percolation threshold as a function of relative particle size with and without affinity.

It can be seen in Table 2 that for $R_H/R_E=1$, $\boldsymbol{\rho_c}$ reproduces the value of 0.1557 (~0.16) from the literature [11, 17]. For $R_H/R_E > 1$, $\boldsymbol{\rho_c}$ grows with R_H/R_E (0.1913, 0.2337), and more so with affinity (0.2368, 0.2870). With only three simulations per case, the coefficient of variance is reasonably small. The average coordination numbers (**c.n.**) are approximately invariant of the affinity and R_H/R_E particle diameter ratio, and are less than an integer away from the number two, since every particle in the conduction path needs a minimum of two contact points to be part of a conductive chain. The average local volume fraction ($\mathbf{p_a}$) correlates well with the critical volume fraction $\mathbf{p_c}$ indicating the **H** and **E** particles are well mixed.

The improvement of percolation threshold is remarkable. By increasing the percolation threshold one could increase the volume fraction of magnetostrictive phase **H** up to nearly $\mathbf{p_c}$, which would result in better performance of the device as measured by the magnetoelectric coupling **k** [13-16]. Without **H-E** particle affinity, $\boldsymbol{\rho_c}$ grows by 22.8 % and 50.0 % for $R_H/R_E=2$, 3, respectively. When **H-E** particle affinity is introduced, the percolation threshold increases by 52.0 % and 84.3 % for $R_H/R_E=2$, 3, respectively. In all cases the percentage change is calculated with respect to the case $R_H/R_E=1$ without affinity, which yields the well-known value $\boldsymbol{\rho_c}$=0.1557 [11, 17].

A typical probability density profile (section 2.3.2) during the gelation stage is shown in Fig. 5. All density profiles show a percent difference less than 8 % (excluding the first and last slice due to edge effects) indicating that the phases remains mixed through all three stages without segregation.

A typical plot of the center of mass (CoM) (described in section 2.3.3) for the **H** particles is shown in Fig. 6. The CoM remains close to the center of the simulation box within 5 % for all simulations in all stages again indicating good mixing without segregation.

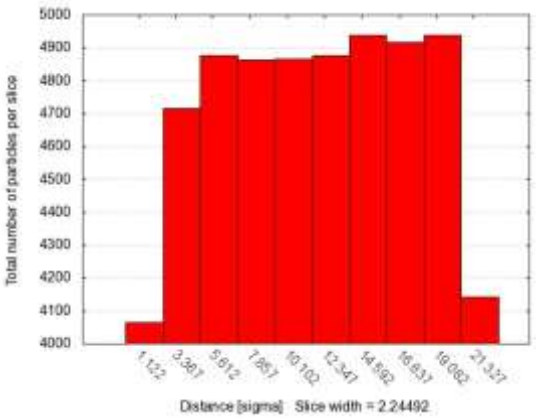

Fig. 5 Probability profile, gelation stage, $R_H/R_E=2$, Type:N, p=0.3

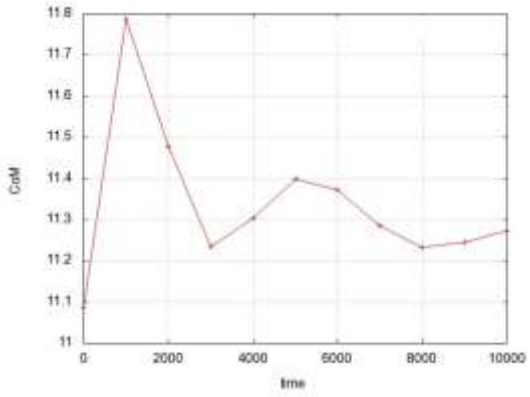

Fig. 6 Center of Mass, gelation stage, $R_H/R_E=2$, Type:N, p=0.3

Renderings of particle positions after each stage of the simulation are shown in Figs. 7-14 with **H** particles in red and **E** particles in blue color. The radial distribution function RDF depicts morphological features and energy plots which attest to the equilibrium reached in each case.

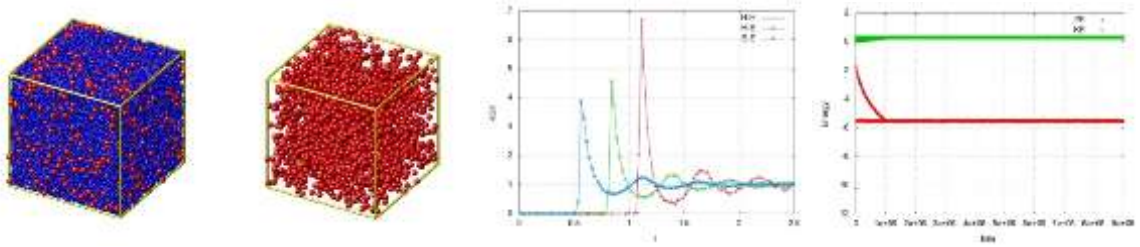

(a) PM:red PE:blue (b) PM only (c) RDF (d) Kinetic and Potential. Energy vs. time

Fig. 7 Mixing stage, $R_H/R_E=2$ p=0.3

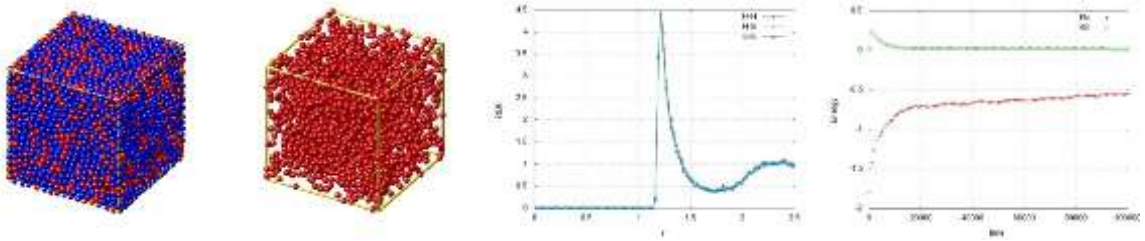

(a) PM:red PE:blue (b) PM only (c) RDF (d) Kinetic and Potential Energy vs. time

Fig. 8 Equilibration stage, $R_H/R_E=1$, Type:N, p=0.3

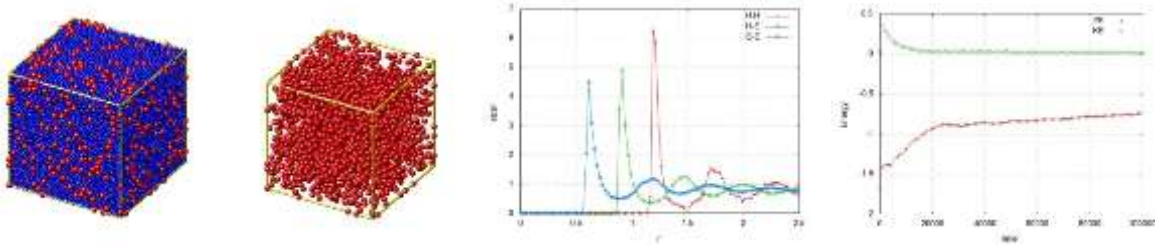

(a) PM:red PE:blue (b) PM only (c) RDF (d) Kinetic and Potential Energy vs. time

Fig. 9 Equilibration stage, $R_H/R_E=2$, Type:N, p=0.3

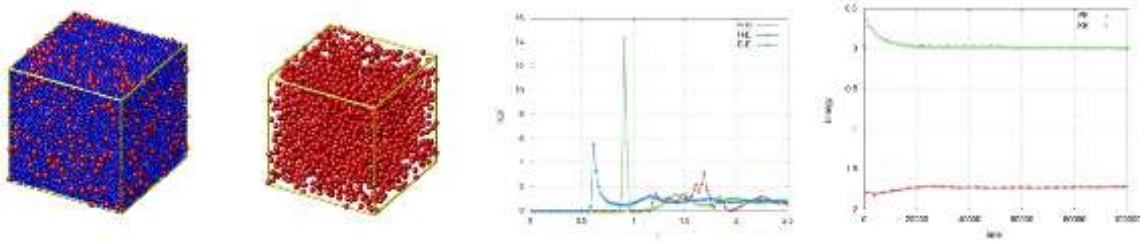

(a) PM:red PE:blue (b) PM only (c) RDF (d) Kinetic and Potential Energy vs. time

Fig. 10 Equilibration stage, $R_H/R_E=2$, Type:A, p=0.3

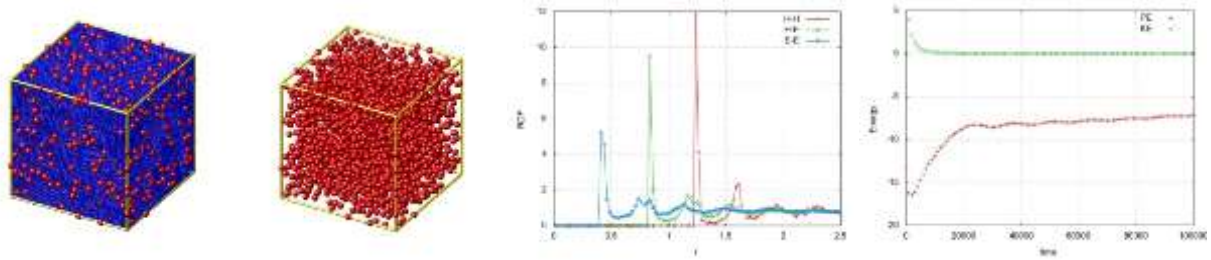

a) PM:red PE:blue (b) PM only (c) RDF (d) Kinetic and Potential Energy vs. time

Fig. 11 Equilibration stage, $R_H/R_E=3$, Type:N, p=0.3

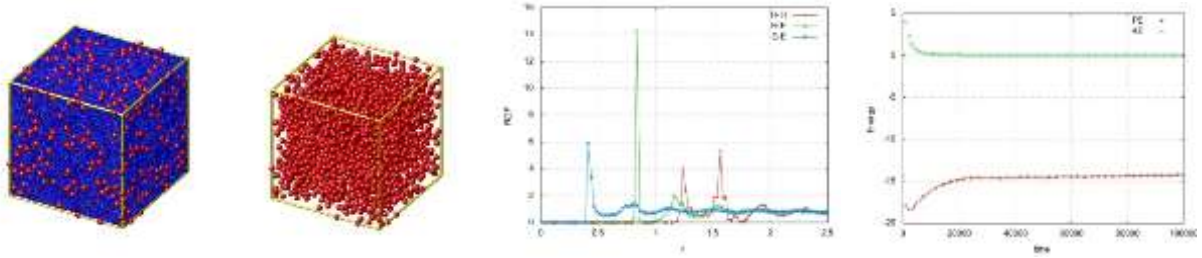

a) PM:red PE:blue (b) PM only (c) RDF (d) Kinetic and Potential Energy vs. time

Fig. 12 Equilibration stage, $R_H/R_E=3$, Type:A, p=0.3

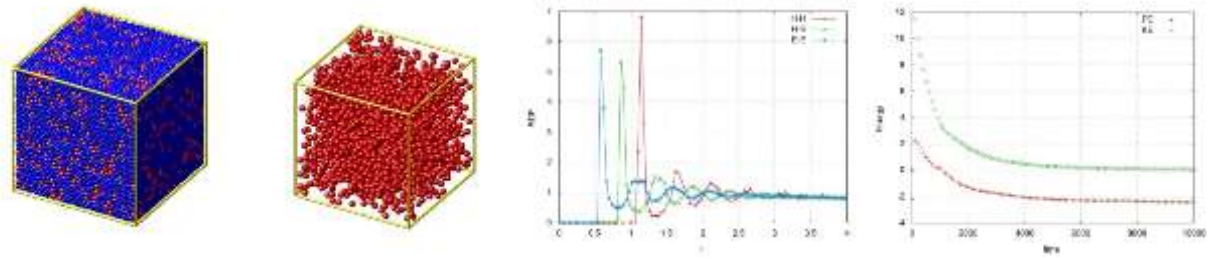

(a) PM:red PE:blue (b) PM only (c) RDF (d) Kinetic and Potential Energy vs. time

Fig. 13 Gelation stage, $R_H/R_E=2$, Type:N, p=0.3

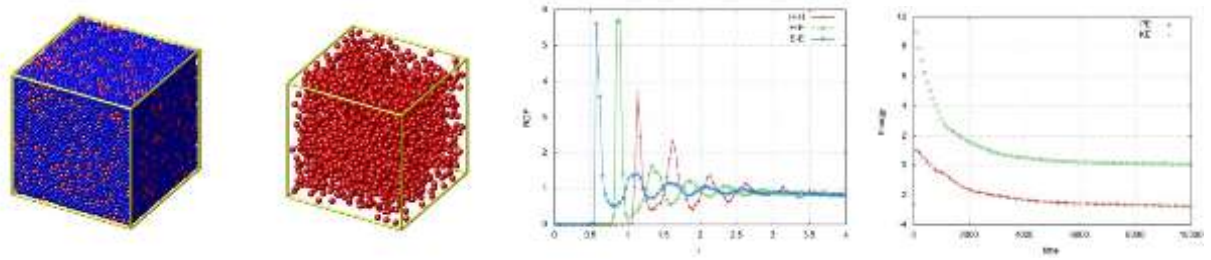

(a) PM:red PE:blue (b) PM only (c) RDF (d) Kinetic and Potential Energy vs. time

Fig. 14 Gelation stage, $R_H/R_E=2$, Type:A, p=0.3

4. Analysis

For the mixing stage when R_H/R_E=2 the RDF for the particle pairs **H-H**, **E-E**, and **H-E** are all as shown in Fig. 7 where the primary peak of H-H interaction occurs at value 1.14σ because there is no segregation and all particles are the same size. In the mixing stage, the packing fraction **f**= 0.5236 is well below the glass transition value **f** = 0.64, 0.675, 0.73 for R_H/R_E = 1, 2, 3 respectively [35, 37]. Further, the potential energy in Fig. 9(d) becomes more negative to reflect the compaction of the powder [22] when the packing fraction **f** is increased.

In Fig. 7, for mixing with R_H/R_E= 2, the RDF abscissa of the primary peaks are separated into three peaks relative to the single peak in Fig. 8. In Fig. 7 the **H-H** peak is at 1.14σ and the **E-E** peak is at 0.58σ, which is roughly half the **H-H** abscissa value. The **H-E** peak is at 0.86σ which is roughly 75 % of the H-H peak location. This is due to the diameters of the E particles being one-half of the **H** particles.

In Fig. 8 for the equilibration stage for R_H/R_E=1, the particles are grown by instantaneously increasing the diameter by factor of $(0.64/0.5236)^{1/3}$, but due to the removal of the periodic boundary conditions (PBC) the effective packing fraction only changes from 0.5236 to 0.5529. In Fig. 9 for the equilibration stage without **H-E** particle affinity and R_H/R_E=2, the potential energy becomes less negative indicating less compression among the spheres as a function of time. That is, the particles find their equilibrium positions because the system has not yet gelled, and this is accompanied by the kinetic energy decreasing to near zero while the temperature is lowered from $0.02\varepsilon/k_B$ to $0.01\varepsilon/k_B$.

To enhance **H-H** particle separation in Figs.10, 12 for the equilibration stage and in Fig. 14 for the gelation stage, particle affinity is introduced between **H** and **E** with no affinity between like particles (**H-H** or **E-E** particles). This changes the radial distribution functions magnifying the vertical height of the **H-E** peaks for all figures, although the location along the abscissa remains the same. In Figs.10, 12, and 14 the **H-E** primary peak is larger than the **E-E** peaks in the same figures because **H-E** affinity introduces some attraction between **H** and **E** phases, as expected. Fig. 9 (no affinity) during equilibration with R_H/R_E = 2 is similar to Fig. 7 (mixing) but the potential energy in Fig. 9(d) becomes less negative indicating that the particles are relaxing to equilibrium.

In the equilibration stage, comparing Figs. 10 and 12 (affinity) to Figs. 9 and 11 (no affinity), there is a sharp increase in the vertical height of the **H-E** peak, and a relative decrease in the **H-H** peak with little change in the **E-E** primary peak. Comparing Fig. 10 (affinity) to Fig. 9 (no affinity) with R_M/R_E = 2, there are three distinct primary peaks in Fig. 9, one for each inter-particle distance **H-H**, **H-E**, and **E-E**, but in Fig. 10 the **H-E** peak only is magnified due to affinity. Comparing Fig. 14 (affinity) to Fig. 13 (no affinity) for R_H/R_E = 3, the **H-E** peak shrinks by about 30 % while the **H-H** peak almost disappears and is distributed among numerous smaller peaks between 1 and 2 on the abscissa shifted to the right. This indicates that the **H** particles have moved away from each other, and this pattern repeats for R_H/R_E = 3. Therefore, with affinity between the **H** and **E** particles, the **H** particles are on average farther apart from each other than they are without affinity, further supporting the results presented in Table 2. In addition, in Figs. 10 and 12 (affinity) the potential energy becomes more negative relative to Figs. 9 and 11 (no affinity). This is because the extended tail of the L-J potential used to model the **H-E** attraction is adding more negative potential energy to the system confirming the **H-E** affinity. These observed relationships between figures 9 through 14 suggest that **E** particles are surrounding the **H** particles, thus isolating the **H** particles from each other, which in turn support the results presented in Table 2 and Fig. 4.

5.0 Summary

Percolation may be interpreted as a combination of two things (a) the number of paths available at each particle node and (b) the probability of success of finding a conductive particle at each node. As the number of paths between nodes increases, the likelihood of success of a percolation from one side of the sample to the other also increases. Likewise, the probability of finding a conductive particle at any given node also increases the likelihood of a successful percolation. These two factors (success per node and paths per node) help us understand how different percolation thresholds occur.

Regarding phase and segregation, when hard shells are under pressure, segregation occurs because of the size, density, or kinetic differences among groups of particles. Liquids do not show this segregation behavior which is only seen with mixing powders [36]. Because particles will not mix as the glass transition is approached [36, 46] , and because particles tend to agglomerate or segregate in response to pressure [36, 46], growing spheres and varying the simulation box size is adopted as a way to control the undesired segregation.

When there is an attractive force between the **H** and **E** particles, the **H** particles become increasingly separated from each other, and this effect becomes more pronounced the greater the size difference between the particles. But, even without **H-E** affinity when the **E** particles are smaller than the **H** particles, percolation is inhibited. Short range affinity can simulate friction to the extent that it prevents small **E** particles from segregating to interstitial locations while long range affinity promotes segregation lowering the percolation threshold.

The radial distribution functions describe inter-particle distances between particles, so when the RDF primary **H-E** peaks are smaller and shifted to the right, the percolation threshold is likely to increase as confirmed by the results. Our research shows two factors that can move the **H-E** peak to the right. The first factor is reducing the size of **E** particles relative to **H** particles to allow **E** particles to move in between and separate the **H** particles thus raising the percolation threshold. The second factor is providing short range affinity between the **H** and **E** particles which inhibits **E** particles from being expelled away from between **H** particles when the composite is compacted. These factors together raise the percolation threshold per Table 2 from f = 0.1557 to f = 0.2870 showing a relative percent increase of 84.3 %.

6. Conclusions

In conclusion, we determined that the percolation threshold increases as the ratio of particles sizes R_H/R_E increases. In addition, we found that the percolation threshold can be increased by inter-phase particle affinity and in fact increases more than in the cases of solely varying particle size. Without **H-E** particle affinity, $\boldsymbol{\rho_c}$ grows by 22.8 % and 50.1 % for R_H/R_E=2, 3, respectively. When **H-E** particle affinity is introduced, the percolation threshold increases by 51.8 % and 84.3 % for R_H/R_E=2, 3, respectively. In all cases the percentage change is calculated with respect to the case R_H/R_E=1 without affinity, which yields the well-known Scher-Zallen value $\boldsymbol{\rho_c}$=0.1557 [23].

In addition, we concur with other investigators [36, 46, 50, 51, 54] that complete mixing and controlling segregation is as critical to percolation as is particle compaction. In particular, we found for the purposes of molecular dynamics simulation, it was necessary to mix the particles with sufficient interstitial space to allow complete mixing, but then to partially compact the particles just below glass transition to allow the particles potential energy to relax before applying final compaction to reach the target packing fractions of 64 %, 67.5 %, and 73 % for R_H/R_E=1, 2, 3 respectively.

This study confirms the hypothesis that both decreasing the particle size of the nonconductive phase relative to the conductive phase and some sort of adhesion and or linking between the conductive and non-conductive phases will maximize the electromechanical contact between the phases while minimizing the undesirable effect of electrical percolation in the conductive phase.

The results of this study were confined to a granular model where all particles were modeled as spheres and particle deformation was minimized (approximating hard-sphere conditions) with a large Leonard-Jones potential energy well depth. Therefore, future studies could involve addressing what happens when the particles deviate from spherical geometry as occurs with sintering and how friction or other adhesive forces affects the conductive phase percolation threshold in magnetoelectric composites. Further studies may involve magnetostrictive or piezoelectric materials made of polymers or the addition of a third phase of polymers or a third particle phase to act as a catalyst or binding agent between **E** and **H** phases.

Acknowledgements

The authors wish to acknowledge use of the West Virginia Super Computing System (Spruce Knob), funded by the National Science Foundation EPSCoR Research Infrastructure Improvement Cooperative Agreement #1003907, without access to which the study would not have been possible.

References

1. W.Eerenstein, N.D.Mathur, J.F.Scott (2006) Multiferroic and magnetoelectric materials. Nature Publishing Group, Dept. Matrl. Sci., Univ. Cambridge, Vol. 442
2. R.Grossinger, G.V.Duong, R.Sato-Turtlli (2008) The physics of magnetoelectric composites. Journal of Magnetism and Magnetic Materials 320: 1972-1977
3. J.Ma, J.Hu, Z.Li, C-W.Nan (2011) Recent progress in multiferric magnetoelectric composites: from bulk to thin films. Adv. Mater 23: 1062-1087
4. M.Bichurin, V.Petrov, S.Priya, A.Bhalla (2012) Editorial multiferric magnetoelectric composites and their applications. Adv. Cond. Matter Phys.12: 129794
5. V.L.O.de Brito, S.A.Cunha, L.V.Lemos, C.B.Nunes (2012) Magnetic properties of liquid-phase sintered $CoFe_2O_4$ for application in magneoelastic and magnetoelectric transducers. Sensors 12:10086-10096
6. Y-H.Chu, L.W.Martin, M.B.Holcomb, M.Gajek, S-J.Han,Q.He, N.Balke, C-H.Yang, D.Lee, W.Hu, Q.Zhan, P-L.Yang, A.Fraile-Rodriquez, A.Scholl, S.X.Wang,R.Ramesh (2008) Electric-field control of local ferromagnetism using magnetoelectric multiferric. Dept. Matrl. Sci. Eng. Univ. CA Berkeley doi: 10.1038/nmat2184
7. C-W.Nan, M-I.S.Song, D.Veichland, G.Srinivasan (2008) Multiferric magnetoelectric composites: historical perspective, status, and future directions. J.Appl.Phys. 103
8. N.Ortega, A.Kumar, J.F. Scott, R.S.Katlyar (2015) Multifunctional magnetostatic materials for device applications. J.Phys: Cond .Matter 27
9. N.S.A.B.Sharif (2015) Synthesis and characterization of lead zirconate titanate ($Pb[Zr_{0.52}Ti_{0.48}]O_3$) properties via high energy planetary ball milling. Ph.D. dissertation, Manufacturing Engineering, University Malaysia Pahang
10. C.A.Randall, N.Kim, J-P.Kucera, W.Cao, T.R.Shrout (1998) Intrinsic and extrinsic size effects in fine grained morphotropic-phase-boundary lead zirconate titanete ceramics. J.Am.Cerm. 81(3):677-688

11. C-W.Nan, Y.Shen, J.Ma (2010) Physical properties of composites near percolation. Annual Review of Materials Research 40: 131-151
12. A.Bunde, W.Deiterich (2000) Percolation in composites, " J. of Electroceramics, 5(2):81-92
13. T.I Muchenik, E.J. Barbero (2014) Micromechanics modeling of magnetoelectric composites. Composites and Advanced Materials, CAMX Conference Proceedings, Orlando FL, Oct 13-16
14. T.I.Muchenik, E.J. Barbero (2015) Charge, voltage and work-conversion formulas for Magnetoelectric laminated composites. Smart Mater, Struct. 24
15. T.I. Muchenik and E.J. Barbero (2016) Magnetoelectric composites, ch. 12 in *Multifunctional composites*, E.J. Barbero (ed), Create Space Independent Publishing, Charleston, SC.
16. T.I.Muchenik, E.J. Barbero (2016) Prediction of extrinsic charge, voltage, and work-conversion factors for laminated magnetoelectric composites. Smart Matter. Struct. 25
17. H.Scher, R.Zallen (1970) Critical density in percolation processes. J.Chem.Phys. 53
18. D.S.Bolintineanu, G.S.Grest, J.B.Lechman, F.Fierce, S.J.Plimpton, P.R.Schunk (2014) Particle dynamics modeling methods for colloid suspensions. Comp. Part. Mech. 1:321-356
19. L.Staron, J.C.Phillips (2015) How large grains increase bulk friction in bi-disperse granular chute flows. Comp. Part. Mech. doi:10.1007/s40571-015-0068-1
20. K.Saitoh, V.Magnanimo, S.Luding (2016) The effects of microscopic friction and size distributions on conditional probability distributions in soft particle packings. Comp. Part. Mech. (vol page TBA)
21. D.C.Rapaport (2014) Molecular dynamics simulation: a tool for exploration and discovery using simple models. J. Phys.:Condens. Matter 26:503104-503121
22. J.Rojek, S.Nosewicz, K.Jursak, M.Chmielewski, K.Bochenek, K.Pietrzak (2015) Discrete element simulation of powder compaction in cold uniaxial pressing with low pressure. Comp. Part. Mech. 3:513-524
23. R.P.Kusy (1977) Influence of particle size ratio on the continuity of aggregates. J. of Appl. Phys. 48
24. K.S.Deepa, S.K.Nisha, P.Parameswaran, M.T.Sebastian, J.James (2009) Effect of conductivity on filer on the percolation threshold of composites. Appl. Phys. Let. 94:142902
25. D.Carrera (2007) Quantum tunneling in chemical reactions. MacMillan Group Meeting 28 Nov.
26. I.S. Beloborodov, A.V.Lopatin, V.M.Vinokur (2005) Coulomb effects and hopping transport in granular metals. Rev. B 72:125121
27. R.T.Hill, J.J.Mock, S.D.Wolter, N.M.Jokest, D.R.Smith, A.Chilkoti (2012) Plasmon ruler with angstrom length resolution," ACS NANO 6(10):9237-9246
28. S.Kadkhodazadeh, J.B.Wagner, H.Kneipp, Katrin Kneipp (2013) Coexistance of classical and quantum plasmonics in large plasmonic structures with subnanometer gaps. Applied Physics Letters 103:083103
29. J.A.Scholl, A.Garcia-Etxarri, A.L.Koh, J.A.Dionne (2013) Observations of quantum tunneling between two plasmonic nanopoles. American Chemical Society Publications, Nano Letter 13:564-569
30. J.Zhang, B.I.Shklovskii (2004) Density of states and conductivity of a granular metal or array of quantum dots. Phys. Rev. B 70:153317
31. J.Li, J-K.Kim (2007) Percolation threshold of conducting polymer composites containing 3D randomly distributed graphite nanoplatlets. Composites Science and Technology 67:2114-2120

32. X. Zhu, (Dec. 2013) Tutorial on Hertz Contact Stress. OPTI 512, https://wp.optics.arizona.edu/optomech/wp-content/uploads/sites/53/2016/10/OPTI-521-Tutorial-on-Hertz-contact-stress-Xiaoyin-Zhu.pdf
33. V.Popov (2010) Contact mechanics and friction. Springer-Verlag, Berlin Heidelberg doi: 10.1007/978-3-642-10803-7_5
34. S. J. Plimpton (1995) Fast parallel Algorithms for short-range molecular dynamics. J. Comp. Phys. 117:1-19
35. G.Foffi, W.Goetz, F.Sciortino, P.Tartaglia, T.Voigtmann (2003) Mixing effects for the structural relaxation in binary hard-sphere liquids. Phys. Rev. Let. 91(8)
36. J.M.Ottino, D.V.Khakhar (2000) Mixing and segregation of granular materials Annual Review. Fluid Mechanics 32:55-91
37. G.Parisi, F.Zamponi (2010) Mean field theory of hard sphere glasses and jamming. Cond. Matt., PACS numbers: 05.20.-y, 61.43.Fs, 64.70.Q-
38. H.J.H.Brouwers (2006) Particle-size distribution and packing fraction of geometric random packing. Phys. Rev. E. 74
39. A.R.Kansal, S.Torquato, F.H.Stillinger (2002) Computer generation of dense polydisperse sphere packing. J. Chem. Phys. 117(18)
40. G.D.Scott, D.M.Kilgour (1969) The Density of Random Close Packing of Spheres. British Journal Applied Physics 2(2)
41. J.C.GRunlan, W.W.Gerberich, L.F.Francis (2001) Lowering the percolation threshold of conductive composites using particulate polymer microstructure. J. of Applied Polymer Science 80:69-705
42. H.M.Hasanabadi, M.Wilhelm, D.Rodrigue (2014) A rheological criterion to determine the percolation threshold in polymer nano-composites, Rheol. Acta 5:869-882
43. R. Eisberg, R.Resnick (1985) Quantum mechanics of atoms molecules solids nuclei and particles. John Wiley and Sons, 2nd Ed.
44. R.L.Kruse (1989) Programming with data structures, Chap. 17, Prentice Hall
45. S. Nappini, Elena Magnano (2015) Surface charge and coating of $CeFe_2O_4$ nanoparticles evidence of preserved magnetic and electronic properties. J.Phys. Chem. C 119:25529-25541
46. K.van der Vaart, P.Gajjar, G.Epely-Chauvin, N.Andreini, J.M.N.T.Gray, C.Ancey (2015) An underlying asymmetry within particle-size segregation/ Phys. Rev. Let. 114: 238001
47. C.P.Royall, S.R.Williams, T.Ohtsuka, J.Tanaka (2008) Direct observation of a local structural mechanism for dynamic arrest. Nature Materials 7 Published online: 22 June 2008; doi:10.1038/nmat2219
48. T.Schilling, S.Dorosz, M.Radu, M.Mathue, S.Jungblut, K.Binder (2013) Mixtures of qnsiotropic and spherical colloids: phase behavior, confinement, percolation phenomena and kinetics. Eur.Phys.J.Special Topics 222:3039-3052
49. M-A.Suarez, N.Kem, W.Kob (2009) Out-of-equilibrium dynamics of a fractal model Gel," J. Chem. Phys. 130:194904
50. A.Amirjanov, K.Sobolev (2008) Optimization of a computer simulation model for packing of concrete aggregates. Particulate Science and Technology 26 (4):380-395
51. A.M.Puertas, M.Fuchs, M.E.Cates (2004) Dynamical heterogeneities close to a colloidal gel. J. Chem. Phys. 121(6)

52. E.Zaccarelli, S.V.Buldyrev, E. La Nave, A.J.Morene, I.Saika-Voivod, F.Sciortino, P.Tartaglia (2005) Model for reversible colloidal gelation. Phys.Rev.Let. 94:218301
53. G.S.Rohr (2001) Structure and bonding in crystalline materials. Cambridge University Press
54. M.Nakagawa, J.L.Moss, S.A.Altobelli (1999) MRI measurements and granular dynamics simulation of segregation of granular mixture. Proceedings of forth microgravity fluid physics and transport phenomena (NASA/CP-199902085526/SUPPL1)
55. D.Stauffer, A.Aharmony (1994) Introduction to Percolation Theory. 2nd Ed. Taylor and Francis London